Global scale analysis and modeling of primary microseisms

L. Gualtieri, E. Stutzmann, C Juretzek, C Hadziioannou, Fabrice Ardhuin

Geophys. J. Int. (2019) **000,** 000–000

Global scale analysis and modeling of primary microseisms

L. Gualtieri[1], E. Stutzmann[2], C. Juretzek[3,4], C. Hadziioannou[3], F. Ardhuin[5]

[1]*Princeton University, Department of Geosciences, Guyot Hall, Princeton, NJ 08540, USA.* (email: luciag@princeton.edu)

[2]*Institut de Physique du Globe de Paris, 1 Rue Jussieu, 75005, Paris, France.*

[3]*Institute of Geophysics, Center for Earth System Research and Sustainability (CEN),*

Universität Hamburg, D-20146 Hamburg, Germany.

[4]*Department of Earth and Environmental Sciences, Ludwig Maximilian University of Munich, D-80333 Munich, Germany.*

[5]*Univ. Brest, CNRS, Ifremer, IRD, Laboratoire d'Océanographie Physique et Spatiale (LOPS), IUEM, Brest, France.*

SUMMARY

Primary microseism is the less studied seismic background vibration of the Earth. Evidence points to sources caused by ocean gravity waves coupling with the seafloor topography. As a result, these sources should be in water depth smaller than the wavelength of ocean waves. Using a state-of-the-art ocean wave model, we carry out the first global-scale seismic modeling of the vertical-component power spectral density of primary microseisms. Our modeling allows us to infer that the observed weak seasonality of primary microseisms in the southern hemisphere corresponds to a weak local seasonality of the sources. Moreover, a systematic analysis of the source regions that mostly contribute to each station reveals that stations on both the East and West sides of the North Atlantic Ocean are sensitive to frequency-dependent source regions. At low frequency (i.e., 0.05 Hz), the dominant source regions can be located thousands of kilometers away from the stations. This observation suggests that identifying the source regions of primary microseisms as the closest coasts can be misleading.

Key words: Seismic noise, Numerical modeling, Computational seismology, Theoretical Seismology.

1 INTRODUCTION

Ambient seismic noise recorded worldwide between about 0.05 and 0.08 Hz is called primary microseism, and it can be generated by ocean gravity waves propagating over the seafloor in shallow water (Hasselmann, 1963). Seismic waves have the same frequency as ocean waves, and therefore primary microseisms are sometimes called single-frequency microseisms. While ambient seismic noise at higher frequencies (secondary microseisms) and lower frequencies (seismic 'hum') has been widely studied, very little has been done about primary microseisms.

Early studies identified sources of primary microseisms in near-shore regions by comparing spectra of microseisms and swells (e.g. Haubrich et al., 1963) or by frequency-wavenumber analysis (e.g. Haubrich & McCamy, 1969; Cessaro, 1994). More recent studies also used beamforming analysis to infer the location of the sources of Rayleigh and Love waves in the primary microseism frequency band (e.g. Juretzek & Hadziioannou, 2016, 2017; Gal et al., 2018). Primary microseisms recorded on the vertical-component seismograms are dominated by the fundamental mode of Rayleigh waves (e.g. Haubrich & McCamy, 1969; Schimmel et al., 2011). The energy ratio between Rayleigh and Love waves on the horizontal components is still under debate and may vary with the location of the seismic station (e.g. Friedrich et al., 1998; Nishida et al., 2008; Juretzek & Hadziioannou, 2017). Several of these studies were conducted assuming that the coast responsible for primary microseism generation was the closest one along the source direction given by the beamforming analysis.

The coupling of surface gravity waves and seafloor topography simplifies in the case of a constant slope (Hasselmann, 1963) or a fine-scale random topography (Ardhuin, 2018). Using the first approach extended to slowly varying topography, Ardhuin et al. (2015) modeled the amplitude of the vertical-component primary microseisms. They showed that the power spectral density (PSD) of primary microseisms could be well modeled at three stations in Europe considering sources in shallow water close to the ocean-continent boundary and assuming a constant ocean-bottom slope and a uniform ocean floor topography along the coast. In that case, ocean waves can be considered to be perpendicular to the topography. Therefore, in agreement with previous theoretical studies (e.g. Hasselmann, 1963; Saito, 2010), they considered ocean waves perpendicular to the topography in shallow water as the main factor responsible for the generation of primary microseism. Small deviations from the perpendicular direction due to 3D topographic effects are not taken into account.

In this paper, we perform the analysis and modeling of one year of continuous seismic data recorded on the vertical component of 24 seismic stations of the Geoscope network located worldwide. We focus on frequencies between 0.05 and 0.08 Hz. In section 2 we describe the analysis workflow applied to our seismic dataset and we detail the method used for modeling seismic PSDs. In section 3, we show maps of sources of primary microseisms, and we compare our modeling with observations

as a function of time and frequency. We also locate the sources that mostly contribute to primary microseisms at each station by inferring the source region that on its own can explain the spectrum of primary microseisms. To asses the robustness of our approach, in Appendix A we present the modeling of another year of data using the same method discussed in Section 2.

2 DATA AND METHOD

We analyze vertical continuous seismic data recorded at 24 seismic stations (triangles in Figure 2) of the Geoscope network in 2013. We use the vertical component long-period (LHZ) seismograms, with a sampling rate of 1 Hz. The instrumental response is deconvolved from raw seismograms in order to get ground displacement, and the PSD (in dB with respect to 1 m^2/Hz) is computed every three hours, considering 50% overlapping time windows of 1024 s. To avoid earthquakes and retain only ambient seismic noise, we keep the minimum value of the PSD every 24 hours.

We model the vertical component PSD at the same 24 seismic stations, following the theoretical framework proposed by Hasselmann (1963) and Ardhuin et al. (2015). To evaluate the location and amplitude of the sources, we use the numerical ocean wave model WAVEWATCH III, version 5.12, as implemented by Ardhuin et al. (2014) with output available at `ftp://ftp.ifremer.fr/ifremer/ww3/HINDCAST`. The model is forced by winds from the European Center for Medium-Range Weather Forecast (ECMWF) every three hours. Extended sources are discretized in a grid of point sources each 0.5° both in latitude and in longitude. The amplitude of the sources is expressed as pressure PSD induced by ocean waves propagating over the seafloor. The ocean wave spectrum is evaluated along the shorelines, and only waves in the direction perpendicular to the shore – both towards and away from the shore – are taken into account (Ardhuin et al., 2015). Following Hasselmann (1963), we do not consider shallow depths that have no nearby coastline.

The simplified model of Ardhuin et al. (2015) based on a large scale sloping seafloor may require unrealistic large bottom slopes where small-scale topographic features (with wavelengths similar to those of ocean waves, typically 50 to 500 m) have large amplitudes (Ardhuin, 2018). The coupling between these topographic features and ocean waves along the perpendicular direction is a possible source of primary microseisms. However, these features are not generally known, making it impossible to take them into account at the global scale. In general, the energy level of ocean waves in directions perpendicular to shore is highly correlated to the energy in other directions so that the theoretical sources used here are a good proxy for general sources caused by all types of bottom topographies. The detailed expression of the pressure PSD $F_p(f)$ [$Pa^2 \cdot m^2 \cdot s$] at the seafloor is given by Ardhuin et al. (2015) (Supplementary materials, equation S22) and in Ardhuin et al. (2019) (Equation 3.16).

In that theoretical model, the source PSD is proportional to an effective slope, called s in Ardhuin

et al. (2015) (expressed in percentage form) and in Ardhuin et al. (2019) (expressed in decimal form), which is not well known in the frequency band of primary microseisms due to uncertainties on bottom topography at scales under 5 km. However, as we shall see in the following, our first-order modeling of primary microseisms does not take into account local site effects at the source (e.g., sediments (e.g. Gualtieri et al., 2015; Koper & Burlacu, 2015), fine-scale seafloor roughness (e.g. Ardhuin, 2018)) and 3D propagation effects (e.g., scattering at the ocean-continent boundary, focusing and defocusing at heterogeneities (e.g. Ziane & Hadziioannou, 2019)). Both of these aspects are not negligible at the frequencies of primary microseisms. Therefore, we define an effective fitting parameter γ (expressed in percentage form), which accounts for effects that are not known (e.g., large-scale bathymetric effects, that is the slope factor s of Ardhuin et al. (2015) and Ardhuin et al. (2019), and small-scale topographic effects as in Ardhuin (2018)) or not taken into account in our modeling (source-site and 3D propagation effects). We point out that our effective fitting parameter γ weakly varies with frequency and therefore can be assumed constant (see section 3.4 for a more detailed explanation). This assumption is justified by the fact that we consider a narrow frequency band (0.05-0.08 Hz) and, as we will see in the next section, the spectrum of primary microseisms expressed in displacement varies within a few dB over this frequency band.

A pressure source acting over a given surface at the ocean seafloor in shallow water is equivalent to a vertical force applied on a flat Earth surface. Assuming a homogeneous half space, the vertical component PSD of the total displacement $u(f)$ [m^2/Hz] recorded at a seismic station at a given time can be written as the integral over the displacement PSDs due to each vertical point force (e.g. Kanamori & Given, 1981):

$$u(f) = \gamma \int_0^{2\pi} \int_0^{\pi} \frac{(2\pi)^2 f c^2}{\rho_c^2 \beta_c^5} F_p(f) \left[\frac{e^{-\frac{\omega \Delta R}{Q(f)U(f)}}}{R sin\Delta} \right] R^2 \sin\phi \, d\lambda \, d\phi \tag{1}$$

where f is the seismic frequency, $\rho_c = 2600$ kg/m^3 is the density of the crust, $\beta_c = 2.8$ km/s is the S-wave velocity in the crust, $R = 6371$ km is the radius of the Earth, Δ is the spherical distance between source and receiver, and λ and ϕ are the longitude and colatitude of the sources, respectively. The adimensional coefficient c accounts for the (resonance) site effect due to the ocean depth at the source (Longuet-Higgins, 1950). We observe that at frequencies between 0.05 and 0.08 Hz and in shallow water, where the sources of primary microseisms are located (Ardhuin et al., 2015), the coefficient c is only relevant to the fundamental mode of Rayleigh waves (c_1 in Longuet-Higgins (1950), his Figure 1) and it is nearly constant with frequency and ocean depth (unlike for secondary microseisms, e.g. Gualtieri et al. (2013)). Therefore, the coefficient c in our computation is set to the corresponding constant value, $c \simeq 0.2$. The attenuation $Q(f)$ and the group velocity $U(f)$ are computed for the fun-

damental mode of Rayleigh waves in the frequency band 0.05–0.08 Hz using the QL6 model (Durek & Ekström, 1996) and the continental version of the PREM model (Dziewonski & Anderson, 1981). The term $e^{-\frac{\omega \Delta R}{Q(f)U(f)}}$ accounts for minor-arc propagation. At the frequencies of primary microseisms, major-arc and multi-orbit propagation can be neglected.

As already discussed, the displacement PSD $u(f)$ depends on the value of the effective fitting parameter γ, which includes effects due to the slope of the seafloor over which ocean waves propagate, as well as local source site effects and propagation effects. While the latter aspects are not included in our first-order modeling, the bathymetric and slope effects are unknown for two main reasons. First, the source magnitude is the result of a complex interference between surface ocean waves and the bottom topography. Second, the ocean floor geometry is generally not known to a level of detail sufficient to estimate the contribution of the slope or the fine-scale bathymetric roughnesses to γ. Therefore, to achieve the first-order modeling of primary microseisms, we estimate an effective fitting parameter γ for each station minimizing the L1 norm between one year of observed and synthetic PSDs, considering their minimum value every 24 hours. Figure 1 shows two examples of the misfit as a function of the effective fitting parameter γ for the station a) CAN (Canberra, Australia) and b) IVI (Ivittuut, Greenland). The minimum misfit (blue dot) is clearly identified in both cases. The effective fitting parameter γ estimated for each station is shown in Figure 3 and listed in Table 1 in the Supplementary Materials.

Assessing an effective fitting parameter γ for each station allows us to perform the first-order modeling of primary microseisms. This parameter includes both local and propagation effects, which cannot be distinguished with the present first-order modeling. In the following section, we will discuss the main outcomes of our modeling. We will also present a strategy to refine the estimate of the effective fitting parameter by inverting for fitting parameters that vary with a given source area.

3 RESULTS

3.1 Worldwide modeling

In Figure 2, we show a map of the median pressure PSD of primary microseisms. The value of the PSD of each source is the median value over 2013 and in the frequency band 0.05–0.08 Hz. We observe that sources on the eastern side of ocean basins at mid-latitudes (i.e., western coasts of Europe and the US) are stronger than sources on the western side. This evidence is due to the prevalence of westerly winds at mid-latitudes. We also observe that many small islands worldwide are associated with sources of primary microseisms.

A few observations of sources of primary microseisms have been documented in the literature by

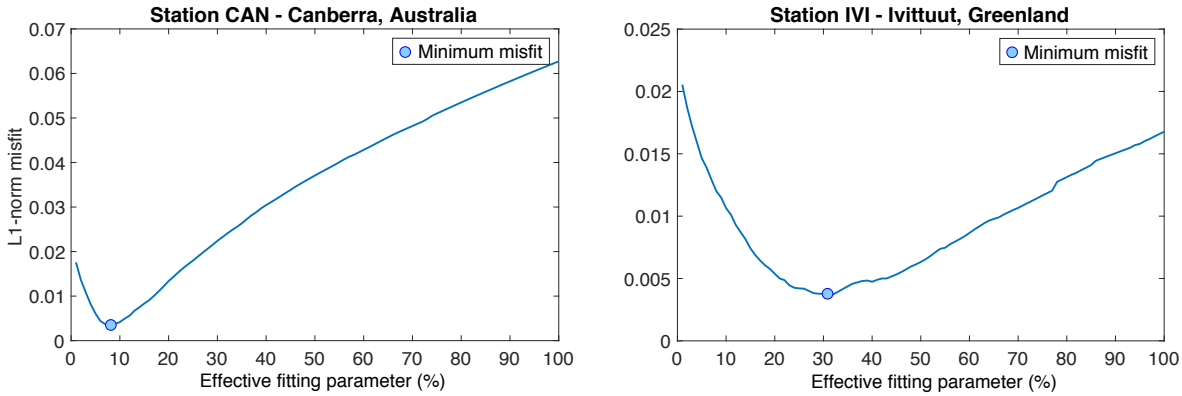

Figure 1. L1-norm misfit between observed and modeled PSDs as a function of the effective fitting parameter γ for the station a) CAN (Canberra, Australia) and b) IVI (Ivittuut, Greenland). The blue dot in each panel highlights the value of the effective fitting parameter γ at which the misfit is minimum.

triangulation of azimuths to the incoming waves. For example, Cessaro (1994) observed persistent primary microseism sources in the North Pacific Ocean near the west coast of the Queen Charlotte Islands (Canada) and the North Atlantic Ocean near the coast of Newfoundland (Canada). In both these regions, the pressure PSD computed from the ocean wave model (Figure 2) shows a large amplitude.

The surrounding insets in Figure 2 show the PSD (in dB with respect to 1 m^2/Hz) as the median over the PSDs computed every 3 hours in 2013 and as a function of frequency. In the case of missing data, we consider only the portion of the synthetics for which we have data. Data are in blue and synthetics in red. Overall, synthetic and observed PSDs have the same amplitude, shape, and slope. The fit between data and synthetic is within a few dB, up to a maximum error of about 4 dB at the station PPTF in French Polynesia. At some stations (e.g., PAF and FOMA in the Indian Ocean) we get a perfect match at all frequencies.

Each synthetic PSD is computed by searching the value of the effective fitting parameter γ that minimizes the L1 norm between continuous observed and synthetic records averaged between 0.05 and 0.08 Hz over the year 2013. The effective fitting parameter γ for each station is shown in Figure 3 (color scale) and Table 1 in the Supplementary Materials. Being affected by source (e.g., local site effects due to sediments and fine-scale seafloor roughness) and propagation effects (e.g., scattering at the ocean-continent boundary, focusing and defocusing at heterogeneities), other than by the slope of the bathymetry at the coast, the effective fitting parameter γ in Figure 3 does not present a simple geographical pattern. However, we can observe small values of γ at stations surrounding the Pacific Ocean (blue triangles), and large values in Europe and Africa (green triangles). A more complex pattern can be observed at seismic stations in the Indian Ocean, where γ is characterized by a large range of values. The effective fitting parameter has an order of magnitude of 10 and it is always larger

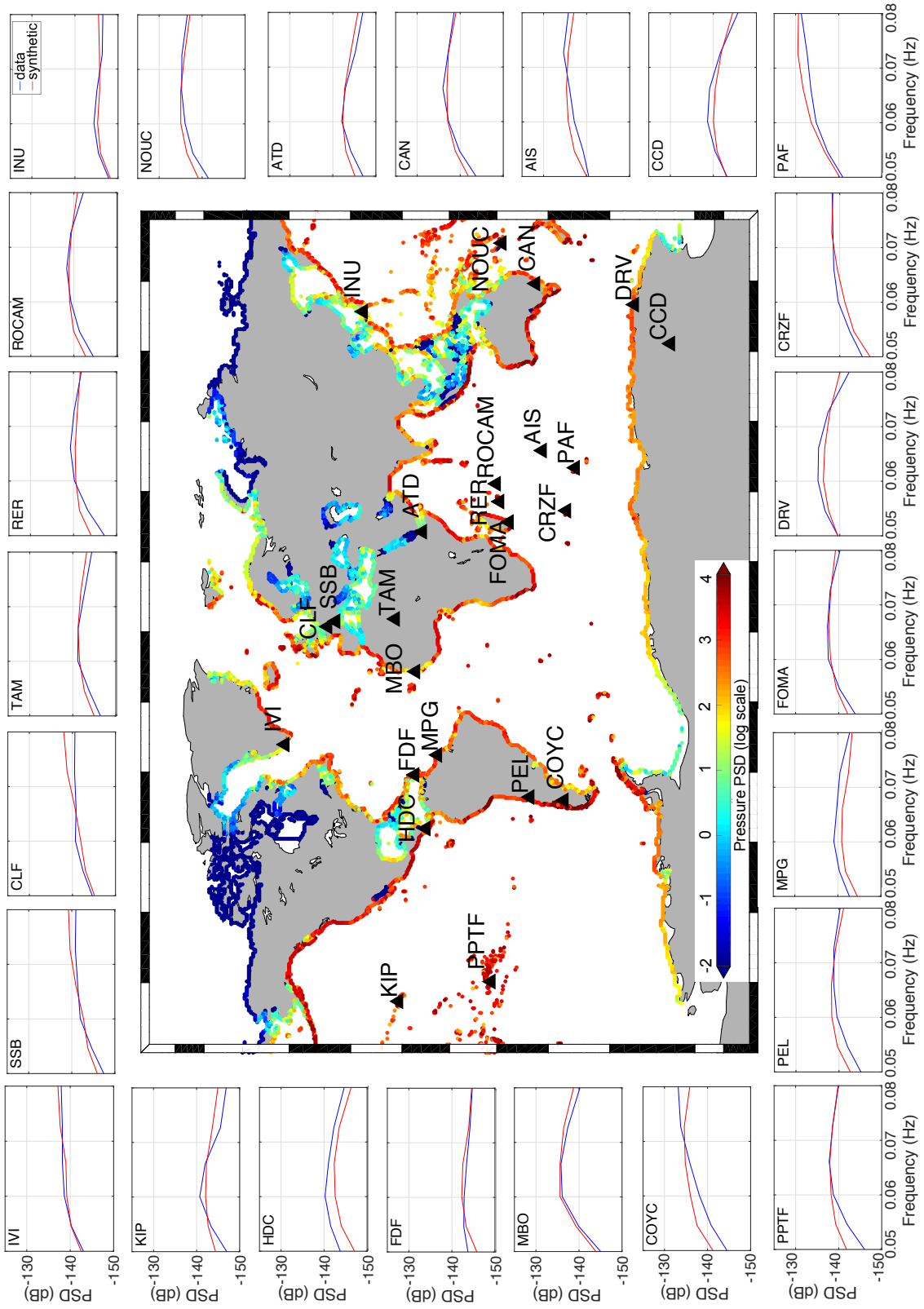

Figure 2. Map (central inset) showing the pressure PSD F_p ($\mathrm{Ps}^2 \cdot \mathrm{m}^2 \cdot \mathrm{s}$, see Equation 1) of primary microseisms in 2013 (color). Pressure PSD is the median over time, integrated between 0.05 and 0.08 Hz. Surrounding insets show the observed (blue) and synthetic (red) seismic displacement PSDs (in dB with respect to 1 m^2/Hz) of primary microseisms as a function of frequency at 24 seismic stations (black triangles in the map) in 2013.

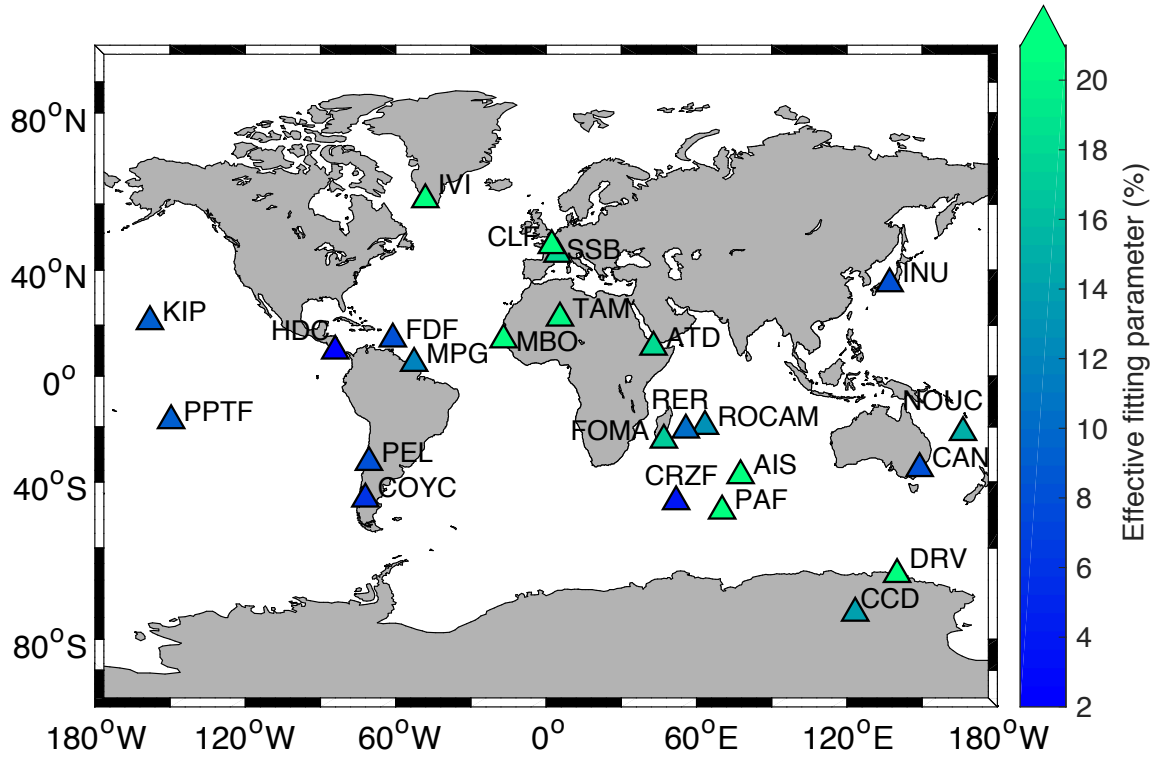

Figure 3. Map showing the effective fitting parameter γ resulting from the L1-norm misfit minimization between observed and synthetic PSDs.

than 1. This means that the features that we do not take into account in our modeling (see Section 2) contribute to the PSD recorded at the seismic stations. In Appendix A, we show that these effective fitting parameters estimated using data in 2013 are time independent, and they allow us to model another year of data with high accuracy.

3.2 Seasonal variations

In Figure 4, we investigate the seasonality of primary microseisms. Figure 4a and 4b show maps of primary microseism sources in January and July 2013, respectively. Sources are defined as the median pressure PSD $F_p(f)$ between 0.05 and 0.08 Hz. In the northern hemisphere, sources are stronger during the local winter (January, Figure 4a) than during the local summer (July, Figure 4b), notably on both East and West sides of the North Atlantic Ocean, on the coasts of Greenland and the Mediterranean Sea. Weaker variability is observed on both sides of the North Pacific ocean. In the southern hemisphere, seasonal variability is less pronounced, with only some confined regions (e.g., Pacific coasts of South America) clearly showing stronger sources during the southern hemisphere winter (July, Figure 4b). The amplitude of sources around Antarctica varies in response to local effects, such

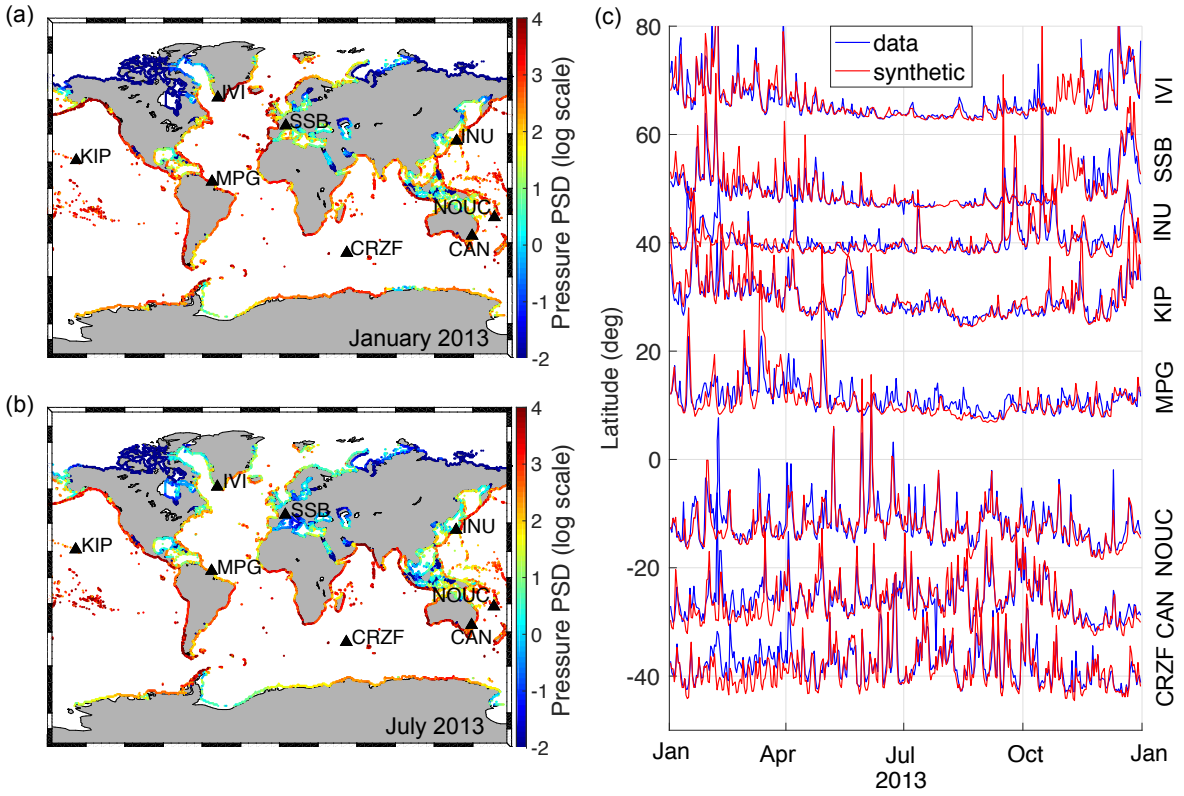

Figure 4. Pressure PSD F_p (Ps$^2\cdot$ m$^2\cdot$ s) of primary microseisms as the median over time and frequency in a) January 2013 and b) July 2013. c) Observed (blue) and synthetic (red) seismic displacement in 2013 at eight seismic stations (triangles in a and b) as a function of time (x-axis). The time series are normalized with respect to the standard deviation at each station and sorted by station latitude (y-axis) to enhance seasonal patterns on both hemispheres. To avoid earthquakes, we keep the minimum value every 24 hours in both data and synthetics. Major peaks and seasonality are well modeled.

as the presence of sea ice, and therefore does not follow a regular seasonal variability, as also observed for secondary microseisms (e.g. Stutzmann et al., 2009; Grob et al., 2011; Stutzmann et al., 2012). A peculiar case is represented by the sources along the coasts of India. Despite being located on the northern hemisphere, they show a larger amplitude in July than in January. As already observed for secondary microseisms (e.g. Koper & de Foy, 2008; Stutzmann et al., 2012; Davy et al., 2015), the sources around India experience a strong seasonality typical of the southern hemisphere.

The seasonality of the sources is reflected in the seasonality of the recorded primary microseisms. Figure 4c shows time series of RMS minimum displacement integrated over the $0.05 - 0.08$ Hz frequency band. We keep the minimum value every 24 hours to remove earthquakes. The time series are plotted as a function of the latitude of the stations (y-axis). The time evolution of data (blue) and synthetics (red) is in good agreement, and many strong peaks are well reproduced by our modeling. Moreover, the ground-displacement time series show a pronounced seasonal variability, especially at

stations in the northern hemisphere, where the amplitude of the primary microseism ground displacement is larger in January-February than in July-August. Stations in the southern hemisphere exhibit less seasonal variability – although we still observe higher ground-displacement in January-February than in July-August – in agreement with the time-varying behavior of the source amplitude in the southern hemisphere. A similar seasonality can be observed in 2017 (see Appendix A, Figure A1a). This evidence is in agreement with observations at the global scale by Schimmel et al. (2011) and in the Indian Ocean by Stutzmann et al. (2009) and Davy et al. (2015), who showed weak seasonal variations of primary microseisms and pronounced seasonal variations of secondary microseisms. The high periodicity of secondary microseisms in the southern hemisphere was also observed in Australia by Aster et al. (2008) using a quantitative metric to asses seasonality over two decades and by Schimmel et al. (2011) by computing the back azimuth to the incoming waves over eight years.

3.3 Dominant source regions

To understand where primary microseisms recorded at each station come from, we perform simulations considering subsets of the sources. We divide the global-scale source distribution into 12 regions, as shown in Figure 5. Then we model the amplitude of the spectrum and the time evolution of the ground displacement considering each one of these source subregions separately. For each station, we use the same effective fitting parameter γ used for the global-scale simulations (Table 1 in the Supplementary Materials). In such a way, a direct comparison with the global scale simulations can be performed. Triangles in Figure 5 denote seismic stations, and their color reflects the dominant source region. Triangles showing two colors represent stations where primary microseisms are due to two different source regions.

Figure 6 shows the median PSD in 2013 (Figure 6a) and the time evolution of the RMS displacement at 0.08 Hz (Figure 6b) and 0.05 Hz (Figure 6c) at the station CAN (Canberra, Australia). Figure 7 shows the same quantities at the station IVI (Ivittuut, Greenland). The color of the solid lines reflects the source subregion (Figure 5) used to compute the synthetic spectra and RMS minimum displacement. Dashed lines denote data (blue) and synthetics computed considering the global-scale distribution of sources (red).

At the station CAN (Figure 6a), sources from all around Australia (black line) dominate at all frequencies, while the contribution of the other regions decreases with distance. This occurs all year round, as shown in Figure 6b at frequency $f = 0.08$ Hz, and in Figure 6c at frequency $f = 0.05$ Hz. We observe that the fit is particularly good at $f = 0.08$ Hz, while at $f = 0.05$ Hz the modeled time series of RMS minimum displacement (dashed red line) shows larger amplitudes than observations

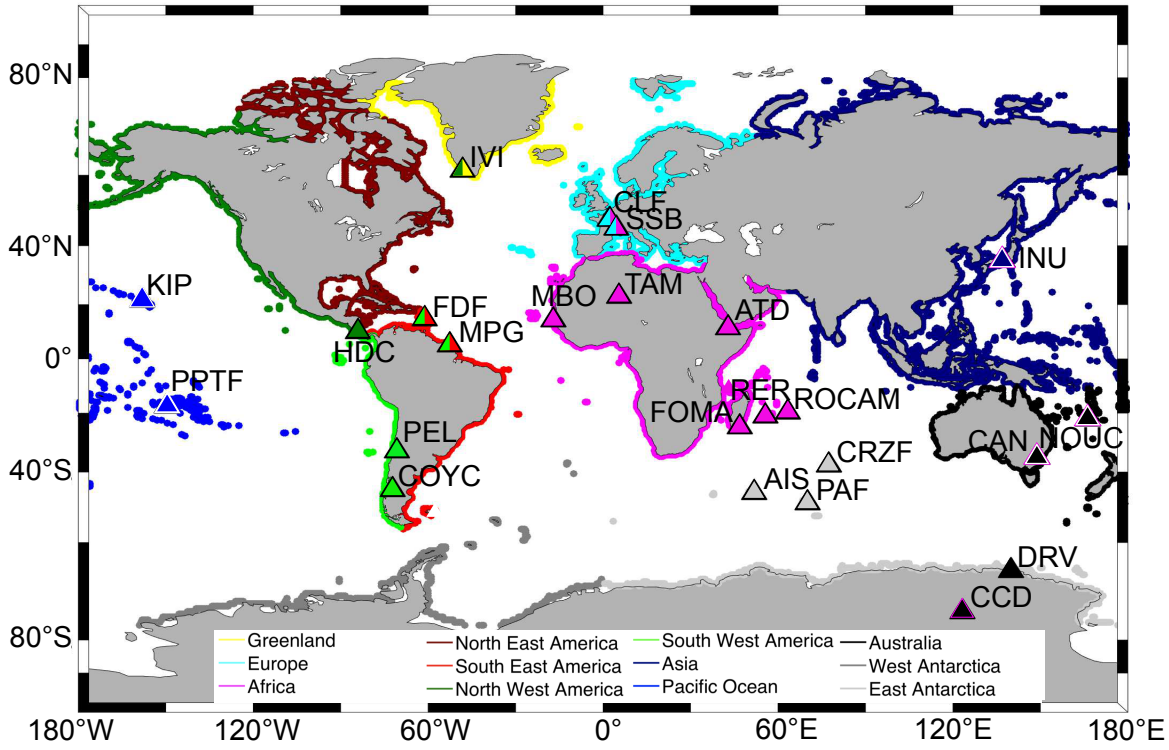

Figure 5. Map showing the 12 chosen source subregions (dots) and the 24 seismic stations (triangles), whose color indicates the dominant source regions.

(blue dashed line), especially during the local winter. The same observation can be made for 2017 (see Appendix A, Figure A2). Detailed investigation of this evidence can be found in section 3.4.

At IVI (Figure 7a), the dominant source region is frequency dependent: sources around Greenland (yellow) give the largest contribution at $f > 0.06$ Hz, and sources on the west coasts of North America dominate at $f < 0.06$ Hz. Although the sources along the east coast of North America (dark red) are located closer to the station IVI, they give a smaller contribution. The time series of RMS minimum displacement at $f = 0.08$ Hz (Figure 7b) due to sources around Greenland (yellow) is the largest contribution throughout the year, with some sporadic dominant contributions due to sources around Europe (e.g., in April). At $f = 0.05$ Hz (Figure 7c), the contribution due to sources on the western (Pacific) coasts of North America (distance beyond 2800 km) is the largest on average, although several individual peaks are due to sources around Greenland (e.g. in May), and Europe (e.g. in November).

Primary microseisms at about 83% of the stations can be explained by a unique source region at all frequencies (color of triangles in Figure 5a and spectra in Figures S1-S4 in the Supplementary materials). Some stations are located in the middle of their dominant source regions (e.g. INU in Japan, TAM in Algeria, KIP and NOUC on islands in the Pacific Ocean), while some others are located close

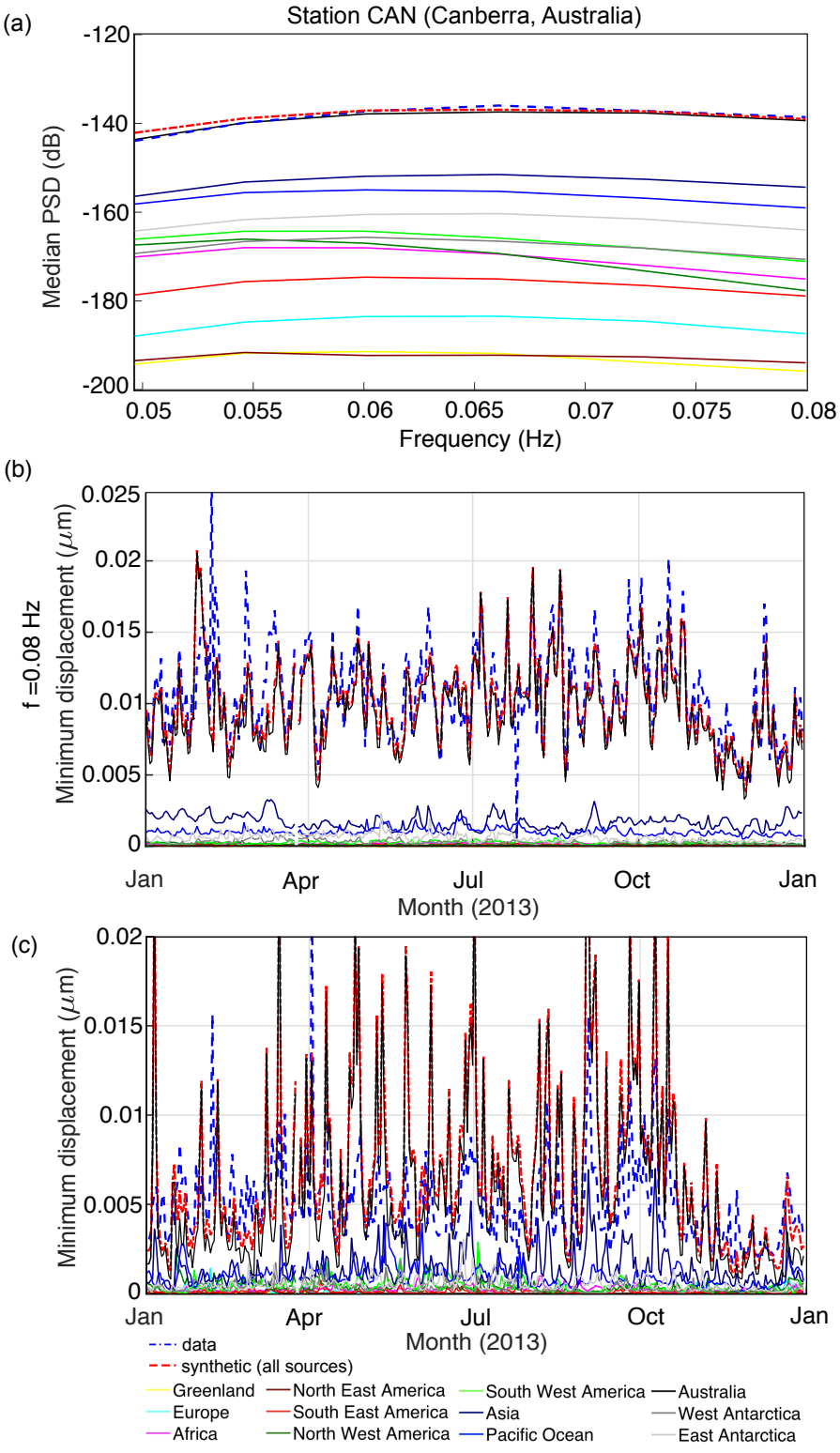

Figure 6. a) Median PSD over 2013 and RMS minimum displacement at the station CAN (Canberra, Australia) at b) 0.08 Hz and c) 0.05 Hz. Solid colored lines are referred to synthetic spectra computed considering only sources in a given subregion (see Figure 5 for the definition of the different subregions). The red dashed line represents the synthetic spectra computed considering sources at the global scale, while the blue dashed line represents data. The legend on the bottom of the figure applies to the three panels. An enlarged version of figures b and c is shown in the Supplementary Materials, in Figures S5 and S6 respectively.

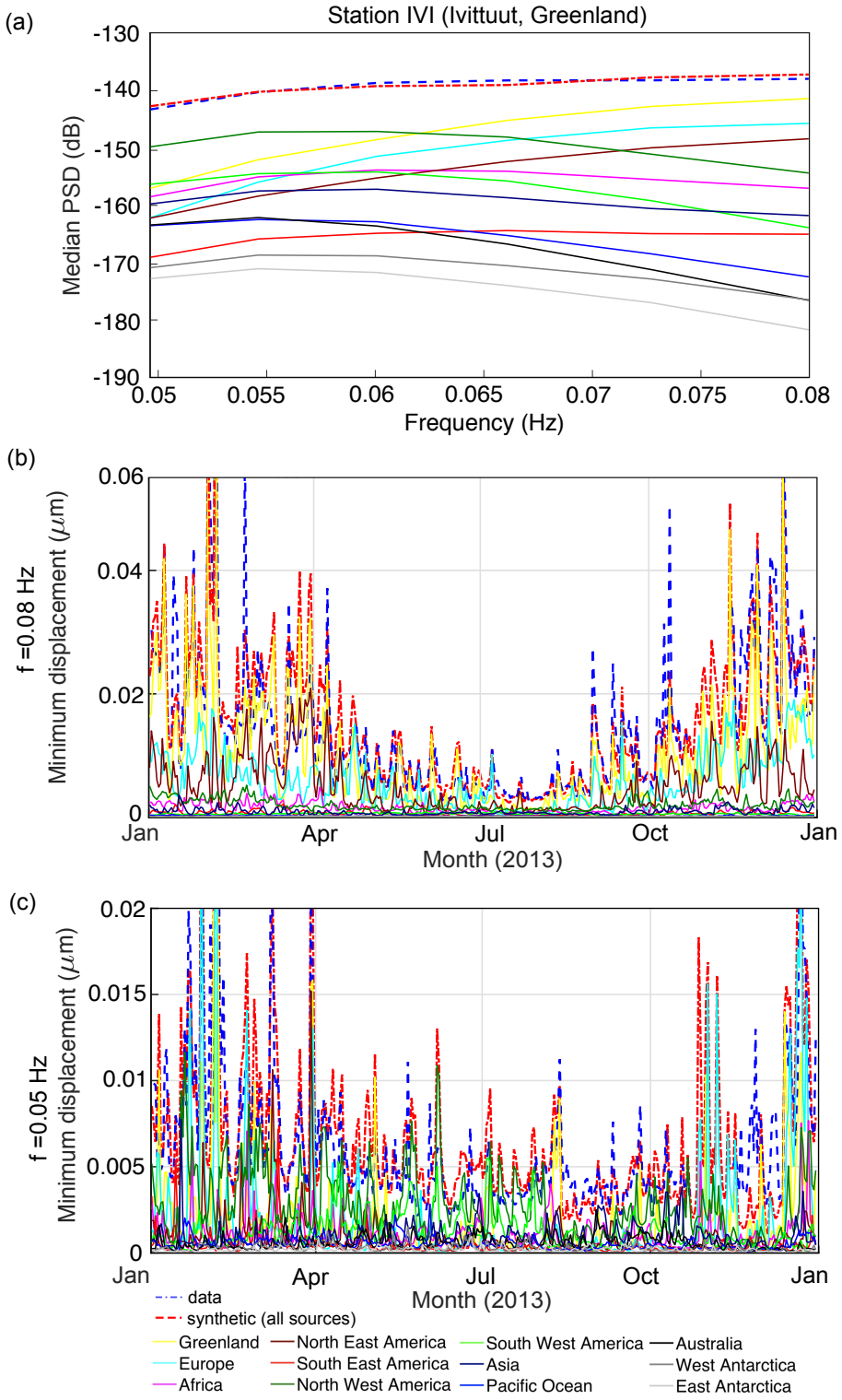

Figure 7. a) Median PSD over 2013 and RMS minimum displacement at the station IVI (Ivittuut, Greenland) at b) 0.08 Hz and c) 0.05 Hz. Solid colored lines are referred to synthetic spectra computed considering only sources in a given subregion (see Figure 5 for the definition of the different subregions). The red dashed line represents the synthetic spectra computed considering sources at the global scale, while the blue dashed line represents data. The legend on the bottom of the figure applies to the three panels. An enlarged version of figures b and c is shown in the Supplementary Materials, in Figures S7 and S8 respectively.

to edge of their dominant source regions (e.g., HDC in Costa Rica, AIS, PAF and CRZF on islands in the Indian Ocean).

On the other hand, primary microseisms at about 17% of the stations – FDF and MPG along the eastern coasts of the central Atlantic, IVI in Greenland, CLF and SSB in France – are characterized by two main dominant source regions for varying frequency (triangles showing two colors in Figure 5 and spectra in Figure S4 in the Supplementary Materials). Some of the stations are characterized by adjacent dominant source regions: SSB and CLF in France where the dominant source regions are Europe and Africa. Primary microseisms at stations in Antarctica, CCD and DRV, show instead dominant sources located around Australia. Some other stations are characterized by local and distant source regions: IVI in Greenland where the dominant source regions are Greenland and the coasts of northwest America, and FDF and MPG along the eastern central Atlantic coasts where the dominant source regions are southeast and southwest America. At high frequency (f$\simeq$ 0.08 Hz), the closest subregion always dominates, while at low frequency (f$\simeq$ 0.05 Hz), it is the subregion located further away that dominates (see Figure 7a and Figure S4). Notably, at low frequency (f$\simeq$ 0.05 Hz), the dominant source region is located beyond about: 2000 km from the station FDF, 2750 km from MPG, 1220 km from CLF, 880 km from SSB, and 2820 km from IVI. This evidence demonstrates that primary microseisms recorded at a seismic station can also be generated at distant coasts, especially around 0.05 Hz.

3.4 Source-dependent effective fitting parameter

In our computations, a constant effective fitting parameter γ has been used for simulating synthetic PSDs at each seismic station. The effective fitting parameter is defined as the value that minimizes the misfit between data and synthetics. In Figures 6 and 7, we observed a remarkably good fit between synthetic and observed minimum displacement all year round. An exception is the station CAN at 0.05 Hz (Figure 6c), for which the synthetic minimum displacement shows a systematic larger amplitude than the observed one. The same discrepancy at 0.05 Hz at CAN is also observed in 2017 (see Appendix A). In Figure S9 and S10 in the Supplementary Materials, we investigate the frequency dependence of the effective fitting parameter. We observe that the parameter γ is weakly frequency dependent at the major part of the stations. In a few cases, the effective fitting parameter varies with frequency (e.g. AIS, NOUC), although the misfit does not vary significantly around the minimum value. As a consequence, the observed overestimation at the station CAN at 0.05 Hz cannot be explained by our assumption of a constant effective fitting parameter.

To investigate this discrepancy between observations and synthetics at 0.05 Hz at the station CAN, we let the effective fitting parameter γ vary over macro source areas of 500 km and we use simulated

annealing to find the local effective fitting parameters that allow a better fit. By iterating over source points, each parameter γ is slightly modified, and changes are accepted if they improve the fit. If the fit worsens, changes are still accepted with decreasing probability for increasing iteration number. The extension of the macro areas, each of which include about 100 source locations, is chosen to reduce the number of parameters and thus the computational time. To resolve detailed local changes of the effective fitting parameter γ, we minimize the L2 norm between data and synthetics.

We allow the local effective fitting parameter to vary symmetrically around the initial constant value used in the previous simulations, that is $\gamma = 8$ for the station CAN (see Figure 3 and Table 1 in the Supplementary materials). Figure 8a shows the RMS minimum displacement obtained for varying the fitting parameter (final model, black) compared to the RMS minimum displacement obtained with a constant effective fitting parameter (initial model, red) and the observed RMS minimum displacement (blue), all at 0.05 Hz. The histograms of the residuals between data and synthetics at 0.05 Hz computed at each time step (Figure 8b) shows that the final model is much closer to the observations (histogram with empty black bars) than the initial model (histogram with light blue bars). The local effective fitting parameter that allows us to obtain the final model reveal a clear spatial pattern, as shown in Figure 8c. With respect to the starting value ($\gamma = 8$), the amplitude of the effective fitting parameter drops on the south-western side of Australia and around New Zealand, it increases on the north-eastern side of Australia and remains unchanged in the Philippine Sea and around Indonesia. Possible causes for this pattern are local structure effects (bathymetry, sediments) and propagation effects (heterogeneities) or other factors in the actual source amplitude that our model does not take into account. For example, we observe that the region where the effective fitting parameter is higher than average (yellow dots in Figure 8c) correlate well with the area of the southwestern Pacific Ocean where tropical cyclones develop. Underestimation of the ECMWF wind forcing in high wind conditions (Pineau-Guillou et al., 2018) (e.g., tropical cyclones) can lead to errors in the ocean wave height (see Figure S11 in the Supplementary Materials and Rascle & Ardhuin (2013)). In turn, hight wind conditions correspond to long period ocean waves, which generate long period seismic noise (0.05 Hz in this case). This can result in an underestimation of the source amplitude in this region (Gualtieri et al., 2018), which would justify the need for a higher effective fitting parameter in our modeling.

4 DISCUSSION AND CONCLUSIONS

In this paper, we showed that our understanding of the generation theory of primary microseisms, combined with state-of-the-art ocean wave models, allows us to model the amplitude of the spectrum of primary microseisms successfully at worldwide-located seismic stations and for varying time.

The pressure source PSD of primary microseisms varies with season, notably in the northern

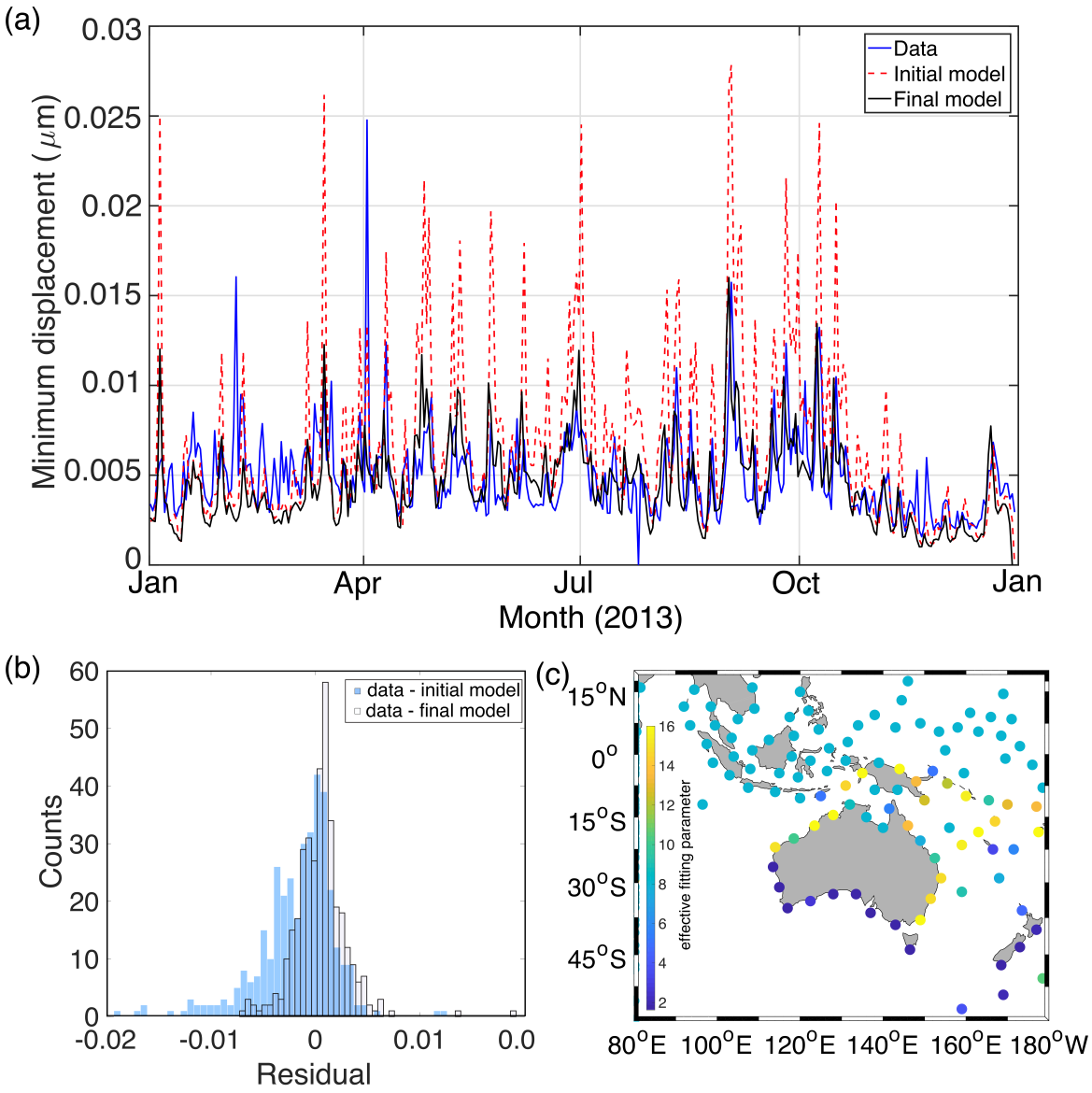

Figure 8. (a) Observed (red) RMS minimum displacement at 0.05 Hz recorded at the station CAN compared to the corresponding synthetic obtained with a constant effective fitting parameter s=8 and to the synthetic obtained varying the effective fitting parameters over macro areas. (b) Histogram of the residuals between data and synthetics (as shown in a) computed with a constant effective fitting parameter (light blue) and a varying effective fitting parameter (black contours). (c) Map showing the effective fitting parameter computed over macro areas of 500 km.

hemisphere. This seasonality is reflected in the seasonality of the recorded displacement as a function of time. The major part of the stations is sensitive to sources located in adjacent subregions, while some of the stations also need source regions located far away to explain the PSD of primary microseisms. For example, the PSD at the station IVI can be explained by sources situated around Greenland at

high frequency ($f > 0.06$ Hz), while they require sources on the western coasts of North America to explain the data at low frequency ($f < 0.06$ Hz). The east coast of North America, the closest coast moving west from IVI, gives a negligible contribution to the actual noise level (see Figure 7a). The same behavior is observed at the stations FDF and MPG, with dominant sources on the eastern coasts of South America at high frequency and on the western coasts of South America at low frequency. The much closer eastern coasts of North America give a negligible contribution (see Figure S4).

One key aspect of the generation of primary microseisms is the slope of the bathymetry in shallow water, where ocean waves propagate. In our modeling, the effect of the slope in shallow water is included in the effective fitting parameter γ (see Figure 3 and Table 1 in the Supplementary materials), which is assessed for each station by minimizing the L1 norm between data and synthetics. This parameter also includes source site effects (e.g., sediments (Gualtieri et al., 2015; Koper & Burlacu, 2015), fine-scale seafloor roughness) and 3D propagation effects (e.g., scattering at the ocean-continent boundary, focusing and defocusing at heterogeneities), which are not taken into account in our 1D modeling. The effective fitting parameter estimated for each station is time independent. The same values can be used to compute synthetics PSDs of primary microseisms during other periods of time (Appendix A). A simple test for sources around Australia recorded at the station CAN at 0.05 Hz – taken as a case study because of the systematic discrepancy between data and modeling – revealed that local variations of the effective fitting parameter can improve the fit between data and synthetics. To investigate this aspect in depth, a regional study will follow.

ACKNOWLEDGMENTS

We thank the GEOSCOPE Observatory and the Incorporated Research Institutions for Seismology (IRIS) for providing openly available seismic data. The output of the ocean wave model can be found at `ftp://ftp.ifremer.fr/ifremer/ww3/HINDCAST`. L.G. acknowledges support from Princeton University. E.S. and F.A. acknowledge support through the ANR Project MIMOSA under Grant ANR-14-CE01-0012. C.J. acknowledges support through the Cluster of Excellence 'CliSAP' (EXC177), Universität Hamburg, funded through the German Science Foundation (DFG). CJ and CH acknowledge support by the Emmy Noether program (HA7019/1-1) of the German Research Foundation (DFG). The authors also wish to acknowledge useful discussions during the TIDES Training Schools, supported by the COST Action ES1401 (European Cooperation in Science and Technology). We thank two anonymous reviewers for their constructive comments that helped to improve the manuscript.

REFERENCES

Ardhuin, F., 2018. Large-scale forces under surface gravity waves at a wavy bottom: A mechanism for the generation of primary microseisms, *Geophysical Research Letters*, **45**(16), 8173–8181.

Ardhuin, F., Rawat, A., & Aucan, J., 2014. A numerical model for free infragravity waves: Definition and validation at regional and global scales, *Ocean Modelling*, **77**, 20–32.

Ardhuin, F., Gualtieri, L., & Stutzmann, E., 2015. How ocean waves rock the Earth: Two mechanisms explain microseisms with periods 3 to 300 s, *Geophysical Research Letters*, **42**(3), 765–772.

Ardhuin, F., Gualtieri, L., & Stutzmann, E., 2019. Physics of ambient noise generation by ocean waves, in *Seismic Ambient Noise*, chap. 3, pp. 69–108, eds Nakata, N., Gualtieri, L., & Fichtner, A., Cambridge University Press.

Aster, R. C., McNamara, D. E., & Bromirski, P. D., 2008. Multidecadal climate-induced variability in microseisms, *Seismological Research Letters*, **79**(2), 194–202.

Cessaro, R. K., 1994. Sources of primary and secondary microseisms, *Bulletin of the Seismological Society of America*, **84**(1), 142–148.

Davy, C., Stutzmann, E., Barruol, G., Fontaine, F. R., & Schimmel, M., 2015. Sources of secondary microseisms in the Indian Ocean, *Geophysical Journal International*, **202**(2), 1180–1189.

Durek, J. J. & Ekström, G., 1996. A radial model of anelasticity consistent with long-period surface-wave attenuation, *Bulletin of the Seismological Society of America*, **86**(1A), 144–158.

Dziewonski, A. M. & Anderson, D. L., 1981. Preliminary reference Earth model, *Physics of the earth and planetary interiors*, **25**(4), 297–356.

Friedrich, A., Krüger, F., & Klinge, K., 1998. Ocean-generated microseismic noise located with the Gräfenberg array, *Journal of Seismology*, **2**(1), 47–64.

Gal, M., Reading, A., Rawlinson, N., & Schulte-Pelkum, V., 2018. Matched field processing of 3 component seismic array data applied to Rayleigh and Love microseisms, *Journal of Geophysical Research: Solid Earth*.

Grob, M., Maggi, A., & Stutzmann, E., 2011. Observations of the seasonality of the antarctic microseismic signal, and its association to sea ice variability, *Geophysical Research Letters*, **38**(11).

Gualtieri, L., Stutzmann, E., Capdeville, Y., Ardhuin, F., Schimmel, M., Mangeney, A., & Morelli, A., 2013. Modelling secondary microseismic noise by normal mode summation, *Geophysical Journal International*, **193**(3), 1732–1745.

Gualtieri, L., Stutzmann, E., Capdeville, Y., Farra, V., Mangeney, A., & Morelli, A., 2015. On the shaping factors of the secondary microseismic wavefield, *Journal of Geophysical Research: Solid Earth*, **120**(9), 6241–6262.

Gualtieri, L., Camargo, S. J., Pascale, S., Pons, F. M., & Ekström, G., 2018. The persistent signature

of tropical cyclones in ambient seismic noise, *Earth and Planetary Science Letters*, **484**, 287–294.

Hasselmann, K., 1963. A statistical analysis of the generation of microseisms, *Reviews of Geophysics*, **1**(2), 177–210.

Haubrich, R. A. & McCamy, K., 1969. Microseisms: coastal and pelagic sources, *Reviews of Geophysics*, **7**(3), 539–571.

Haubrich, R. A., Munk, W. H., & Snodgrass, F. E., 1963. Comparative spectra of microseisms and swell, *Bulletin of the Seismological Society of America*, **47**, 111–127.

Juretzek, C. & Hadziioannou, C., 2016. Where do ocean microseisms come from? A study of Love-to-Rayleigh wave ratios, *Journal of Geophysical Research: Solid Earth*, **121**(9), 6741–6756.

Juretzek, C. & Hadziioannou, C., 2017. Linking source region and ocean wave parameters with the observed primary microseismic noise, *Geophysical Journal International*, **211**(3), 1640–1654.

Kanamori, H. & Given, J. W., 1981. Use of long-period surface waves for rapid determination of earthquake-source parameters, *Physics of the Earth and Planetary interiors*, **27**(1), 8–31.

Koper, K. D. & Burlacu, R., 2015. The fine structure of double-frequency microseisms recorded by seismometers in North America, *Journal of Geophysical Research: Solid Earth*, **120**(3), 1677–1691.

Koper, K. D. & de Foy, B., 2008. Seasonal anisotropy in short-period seismic noise recorded in south asia, *Bulletin of the Seismological Society of America*, **98**(6), 3033–3045.

Longuet-Higgins, M. S., 1950. A theory of the origin of microseisms, *Philosophical Transactions of the Royal Society A*, **243**(857), 1–35.

Nishida, K., Kawakatsu, H., Fukao, Y., & Obara, K., 2008. Background Love and Rayleigh waves simultaneously generated at the Pacific Ocean floors, *Geophysical Research Letters*, **35**(16), L16307.

Pineau-Guillou, L., Ardhuin, F., Bouin, M.-N., Redelsperger, J.-L., Chapron, B., Bidlot, J.-R., & Quilfen, Y., 2018. Strong winds in a coupled wave–atmosphere model during a north atlantic storm event: evaluation against observations, *Quarterly Journal of the Royal Meteorological Society*, **144**(711), 317–332.

Rascle, N. & Ardhuin, F., 2013. A global wave parameter database for geophysical applications. Part 2: Model validation with improved source term parameterization, *Ocean Modelling*, **70**, 174–188.

Saito, T., 2010. Love-wave excitation due to the interaction between a propagating ocean wave and the sea-bottom topography, *Geophysical Journal International*, **182**(3), 1515–1523.

Schimmel, M., Stutzmann, E., Ardhuin, F., & Gallart, J., 2011. Polarized Earth's ambient microseismic noise, *Geochemistry, Geophysics, Geosystems*, **12**(7).

Stutzmann, E., Schimmel, M., Patau, G., & Maggi, A., 2009. Global climate imprint on seismic noise, *Geochemistry, Geophysics, Geosystems*, **10**(11), Q11004.

Stutzmann, E., Ardhuin, F., Schimmel, M., Mangeney, A., & Patau, G., 2012. Modelling long-term

seismic noise in various environments, *Geophysical Journal International*, **191**(2), 707–722.

Ziane, D. & Hadziioannou, C., 2019. The contribution of multiple scattering to Love wave generation in the secondary microseism, *Geophysical Journal International*, **217**(2), 1108–1122.

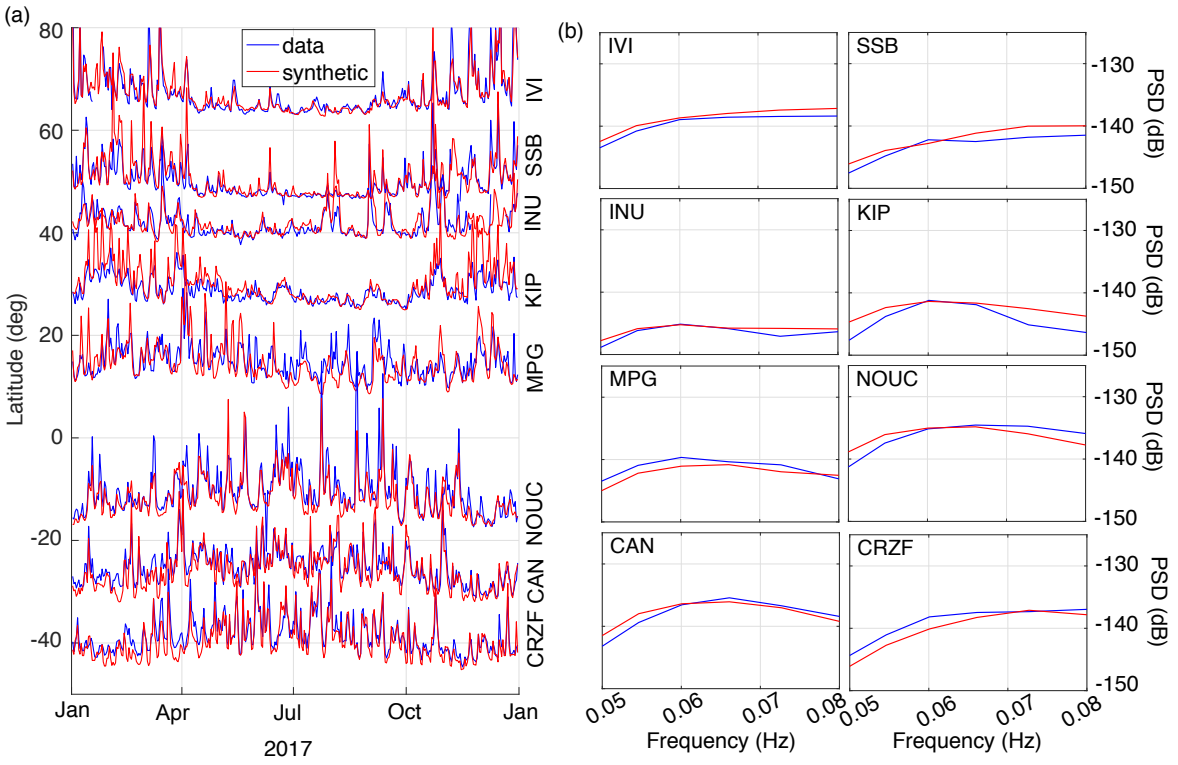

Figure A1. (a) Observed (blue) and synthetic (red) seismic displacement in 2017 as a function of time (x-axis). Time series are normalized with respect to the standard deviation at each station and sorted by station latitude (y-axis). (b) Observed (blue) and synthetic (red) seismic displacement PSDs (in dB with respect to 1 m^2/Hz) of primary microseisms in 2017 as a function of frequency. Synthetics have been computed using the same empirical fitting parameters γ found minimizing the misfit between data and synthetics in 2013 (Figure 3, and Table 1 in the Supplementary Materials). The location of the seismic stations is shown in Figures 4a and 4b.

APPENDIX A: MODELING PRIMARY MICROSEISMS RECORDED IN 2017

To evaluate whether our results vary over time and assess the robustness of the effective fitting parameter, we compute synthetic PSDs in 2017 using the same effective fitting parameters estimated using data in 2013 (Table 1 in the Supplementary Materials and Figure 3).

Figure A1 show the comparison between data (blue) and synthetics (red) at eight stations of the Geoscope network. The location of the stations is shown in Figure 4. Figure A1a shows time series of RMS minimum displacement integrated between 0.05 and 0.08 Hz. As in Figure 4c for 2013, the time series in 2017 in Figure A1a are plotted as a function of station latitude (y-axis). The time evolution and the strongest peaks in the data are well reproduced by the synthetics. Like in 2013, we observe a pronounced seasonality at stations in the northern hemisphere.

Figure A1b shows the PSD (in dB with respect to 1 m^2/Hz) as the median value of the PSDs computed every 3 hours in 2017 and as a function of frequency. Data are in blue and synthetics in red.

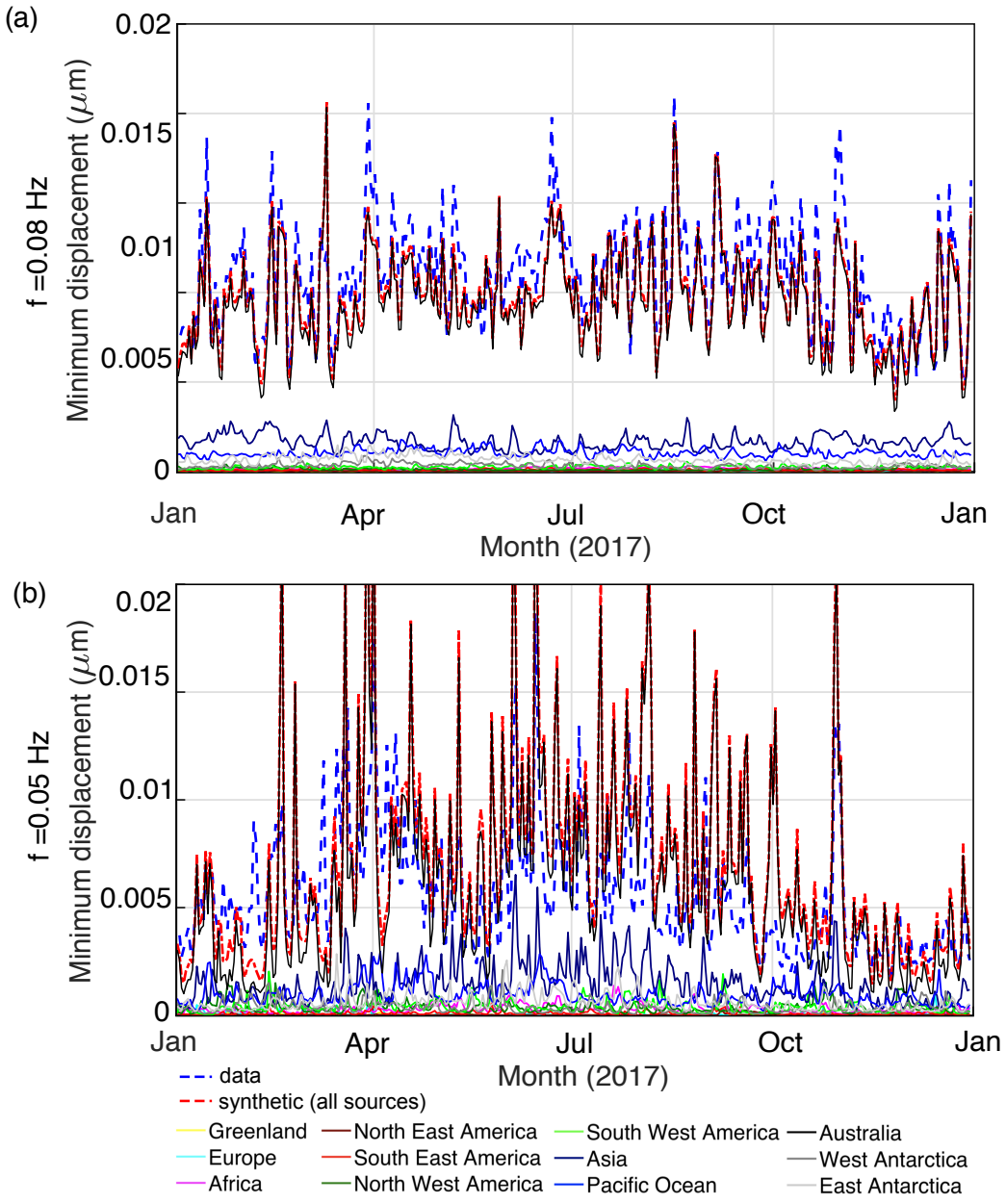

Figure A2. RMS minimum displacement at the station CAN (Canberra, Australia) in 2017 at a) 0.08 Hz and b) 0.05 Hz. Solid colored lines are referred to synthetic spectra computed considering only sources in a given subregion (see Figure 5 for the definition of the different subregions). The red dashed line represents the synthetic spectra computed considering sources at the global scale, while the blue dashed line represents data.

The overall shape and amplitude of the PSD are well reconstructed at all stations, with a fit within a few dB. We recall that the same effective fitting parameters found in section 2 using data in 2013 have been used to compute synthetics in 2017.

We also investigate the RMS of the displacement at the station CAN in 2017 for varying frequency. Similarly to 2013 (Figures 6b and 6c), we find that the fit between data and synthetics is particularly

good at $f = 0.08$ Hz (Figure A2a), while at $f = 0.05$ Hz (Figure A2b) the modeled time series (dashed red line) shows larger amplitudes than observations (blue dashed line). This persistent overestimation could indicate a recurrent overestimation of the source amplitude in this region (for example associated with tropical cyclones, see section 3.4) or to features that have been not taken into account in our modeling (e.g., sediments at the source).